



Cite this: *J. Mater. Chem. A*, 2024, **12**, 28247

In search of widening the electrochemical window of solid electrolytes for Li-batteries: the $\text{La}_{0.29}\text{Li}_{0.12+x}\text{M}_{1-x}\text{Zr}_x\text{O}_3$ ($\text{M} = \text{Nb, Ta}$) perovskite-type systems[†]

Ester García-González, ^a Rafael Marín-Gamero, ^a Miguel Kuhn-Gómez, ^a Alois Kuhn, ^b Flaviano García-Alvarado ^b and Susana García-Martín ^{*a}

All solid-state batteries (ASSBs) are required to address challenges of the last generation of Li-batteries such as advances in safety performance, energy density and battery life. Progress of Li-ASSBs requires the development of solid electrolytes with high Li-conductivity and wide electrochemical window. The $\text{La}_{(2/3)-x}\text{Li}_{3x}\text{TiO}_3$ (LLTO) oxides present the highest "bulk" Li-conductivity among the electrolytes with perovskite structure but present significant grain boundary effects that decrease the total conductivity and confer poor electrochemical stability. The oxides of the $\text{La}_{(1/3)-x}\text{Li}_{3x}\text{NbO}_3$ system (LLNO) present slightly lower reduction voltages than the LLTO-oxides and similar values of total conductivity. We have studied the $\text{La}_{0.29}\text{Li}_{0.12+x}\text{Nb}_{1-x}\text{Zr}_x\text{O}_3$ (LLNZO) and $\text{La}_{0.29}\text{Li}_{0.12+x}\text{Ta}_{1-x}\text{Zr}_x\text{O}_3$ (LLTaZO) systems with the aim of increasing the Li-conductivity and electrochemical stability of perovskite-based electrolyte oxides. Conductivity values as high as in LLNO are found in the LLNZO system but somewhat lower in the LLTaZO system. However, the electrochemical window of these new solid electrolytes is remarkably wide, in particular in the $\text{La}_{0.29}\text{Li}_{0.17}\text{Ta}_{0.95}\text{Zr}_{0.05}\text{O}_3$ compound, which is stable between 1.35 and 4.8 V vs. Li^+/Li .

Received 31st July 2024
Accepted 16th September 2024

DOI: 10.1039/d4ta05326e
rsc.li/materials-a

Introduction

Li-ion batteries (LIBs) are currently the most advanced energy storage systems for portable electronic devices, such as mobile phones and computers, due to their high gravimetric/volumetric energy density, high flexibility of geometry, long cycle life, and low self-discharge. However, the complete introduction of LIBs in the growing fields of electric vehicles and grid energy storage requires improvements in safety and cost reduction. Commercial LIBs use flammable organic liquid electrolytes that decompose when high voltage electrodes are used. On the other hand, these electrolytes react with anodes at low voltage to form a lithium-ion permeable passivation layer, the solid electrolyte interphase (SEI), and consume lithium. In the best cases, the SEI is stable and does not consume any more lithium after the first discharge. At worst, the destruction and formation of the SEI during cycling will deplete the electrolyte of

lithium and shorten the battery life. In this context, all solid-state batteries (ASSBs) using a thin solid electrolyte are required to address safety and coulombic efficiency issues while increasing energy density. Despite considerable advances in ASSBs that have been achieved during the past few decades, several challenges still exist that hinder their practical applications and commercialization.¹ Progress of Li-ASSBs requires the development of solid electrolytes with high Li-conductivity, negligible electronic conductivity, wide electrochemical window, and chemical compatibility with the electrodes. A variety of inorganic oxides and sulfides, as well as polymers have been investigated as solid electrolytes for Li-ASSBs.^{2–5} In general, sulfides exhibit higher total conductivity with low grain-boundary resistance and higher mechanical robustness than oxides. However, the electrochemical window of oxides is significantly wider due to their high oxidation potential (in some cases above 4.0 V). First-principles calculations suggest that this high voltage stabilization is not thermodynamically intrinsic but is associated with slow kinetics of decomposition reactions that lead to the formation of passivation layers at the interface, which inhibit further decomposition of the electrolyte.⁶ In addition to oxides and sulfides, newly emerging halide solid state electrolytes have recently been intensively studied for application in ASSBs due to their favorable combination of high ionic conductivity, high chemical and electrochemical stability,

^aDepartamento de Química Inorgánica I, Facultad de Ciencias Químicas, Universidad Complutense, 28040 Madrid, Spain. E-mail: sgmartin@ucm.es

^bDepartamento de Química y Bioquímica, Facultad de Farmacia, Universidad San Pablo-CEU, CEU Universities, Urbanización Montepríncipe, Boadilla del Monte, E-28668, Madrid, Spain

[†] Electronic supplementary information (ESI) available: Details about Le Bail analysis, atomic percentages by XEDS, and impedance spectroscopy graphics and data of the cells. See DOI: <https://doi.org/10.1039/d4ta05326e>



and superior mechanical deformability.⁷ Regarding oxides, garnet-type, and perovskite-type Li-oxides are considered among the most promising (and most explored) solid electrolytes. In general, lithium-garnet oxides exhibit excellent stability against Li metal concluded by their low reduction potential *versus* Li⁺/Li (0.05 V in the case of Li₇La₃Zr₂O₁₂). However, these compounds are air-sensitive to the atmosphere (moisture and CO₂) which greatly affects their application as electrolytes. In contrast, lithium-perovskite oxides present higher chemical stability although higher reduction potential. Perovskite-type oxides (ABO₃ stoichiometry) have been widely investigated since Li-ion conductivity as high as $\approx 1 \times 10^{-3}$ S cm⁻¹ at room temperature was reported in 1993 in a compound of the family La_{(2/3)-x}Li_{3x}TiO₃ (LLTO) that contains A-cation vacancies.⁸ Despite their high bulk Li-conductivity, the LLTO-oxides present large grain boundary resistances that significantly decrease the total conductivity. Besides, these electrolytes have a relatively narrow electrochemical window because intercalation of Li with reduction of Ti⁴⁺ occurs at about 2 V.⁹⁻¹¹ Several systems have been developed by substituting other transition metals for Ti to widen the electrochemical window and/or to decrease the grain boundary resistance.¹²⁻¹⁹ The current interest seems to be focused on Li-perovskites of transition metals of the second and third rows of the periodic table, mainly on Nb-perovskites with low grain boundary resistances leading to total Li-conductivity in the range from 10⁻⁴ to 10⁻⁵ S cm⁻¹ at room temperature and reduction potentials *vs.* Li⁺/Li lower than 2 V.

In this context, following initial reports, the study of the system La_{(1/3)-x}Li_{3x}NbO₃ regained a great deal of attention.²⁰⁻²² The range of existence of the solid solution corresponds to $0 \leq x \leq 0.06$ and the oxide with the highest ionic conductivity is the one of composition La_{0.29}Li_{0.12}NbO₃ ($x = 0.04$).¹³ In addition to the slight reduction of the intercalation voltage compared to the LLTO-oxides, the Nb-perovskites have the benefit that they show similar values of grain boundary and bulk resistances,^{13,22} contrary to the Ti-perovskites that, as mentioned above, present high grain boundary resistances, which have been attributed to lithium depletion in the space charge region.²³ However, the bulk ionic conductivity in the titanates still is higher than in the niobates, which might be related to differences in the crystal structure, in particular in the location of the cation vacancies that contribute to the Li-motion paths. The average crystal structure of oxides of La_{(2/3)-x}Li_{3x}TiO₃ system contains (00l)-layers of La atoms alternating with (00l)-layers of Li and La atoms and vacancies along the [001] direction of the crystal structure.²⁴ In the oxides of the La_{(1/3)-x}Li_{3x}NbO₃ system, (00l)-layers of cation vacancies (empty crystallographic positions), which probably do not contribute to the Li-motion, alternate with (00l)-layers containing La, Li, and vacancies (Fig. 1).²⁵ In addition to the ordering of these empty positions along the [001] direction, a modulation of the crystal structure associated with the La/Li/vacancies planes has been revealed by transmission electron microscopy, a likely additional barrier to the Li motion.²⁵⁻²⁷ The La_{(1/3)-x}Li_{3x}TaO₃ system has been less explored although previous studies report that these oxides present a similar average crystal structure to the corresponding Nb-

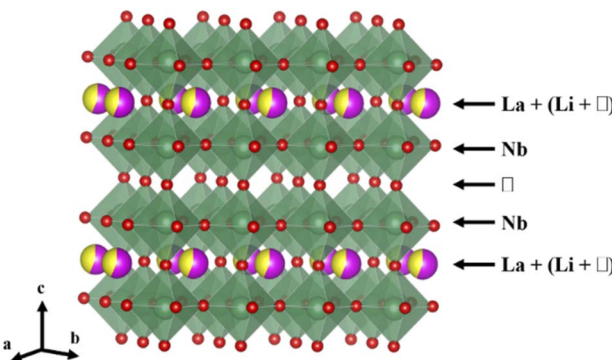


Fig. 1 Schematic representation of the crystal structure of La_{(1/3)-x}Li_{3x}NbO₃ oxides.

oxides and that the highest ionic conductivity, although lower than in the Nb system, is achieved for the compound with $x = 0.06$.²⁸

We report in this article the study of La_{0.29}Li_{0.12+x}Nb_{1-x}Zr_xO₃ and La_{0.29}Li_{0.12+x}Ta_{1-x}Zr_xO₃ systems. The $x = 0$ compounds correspond to the stoichiometry with the highest conductivity of the niobates.¹³ The aim of this work is to improve the ionic conductivity, compared to the La_{0.29}Li_{0.12}MO₃ oxides (M = Nb, Ta), by increasing the Li content. In this sense, the substitution of Nb⁵⁺ (or Ta⁵⁺) by Zr⁴⁺ requires an increase of Li⁺ cations within the A-positions of the crystal structure, decreasing the high concentration of ordered cation vacancies and, in principle, favoring the less ordered structure of the Ti-system. Furthermore, replacing Nb(Ta) with Zr is expected to widen the electrochemical window of the electrolytes.

Experimental section

Synthesis

La_{0.29}Li_{0.12+x}Nb_{1-x}Zr_xO₃ and La_{0.29}Li_{0.12+x}Ta_{1-x}Zr_xO₃ oxides with $0.05 \leq x \leq 0.2$ have been prepared by the conventional ceramic method using Li₂CO₃ (Sigma-Aldrich $\geq 99.00\%$), La₂O₃ (Sigma-Aldrich 99.99%), Nb₂O₅ (Sigma-Aldrich 99.99%), Ta₂O₅ (Sigma-Aldrich 99.00%) and ZrO₂ (Riedel-de Haen A.G. pure). La₂O₃ was dried at 1173 K prior to weighing in order to eliminate La(OH)₃. Stoichiometric amounts of the starting materials were mixed and heated at 1173 K in air to decompose the lithium carbonate. Afterwards, the samples were pelletized and heated at 1523 K in air for 48 h with intermediate grindings. The pellets were covered with a powder of the same composition to avoid Li-losses. Fast cooling of the samples was carried out by taking them out of the furnace at 1523 K to avoid A-cation ordering. The La_{0.29}Li_{0.12}NbO₃ (LLNO) composition was also prepared and studied for comparison with previous reports.¹³

Crystal structure characterization

The initial crystalline phase identification was carried out by powder X-ray diffraction (PXRD) using a PANalytical X'PERT PRO MPD diffractometer with Cu K α radiation and X'PERT PEAPD software. The patterns were recorded in step mode with



a step size equal to 0.02 (2 θ degrees) and time per step equal to 10 s. Le Bail fitting of the XRD patterns was performed to obtain the lattice parameters of the phases in every sample using Fullprof software.^{29,30}

For transmission electron microscopy (TEM) studies, the compounds were ground in *n*-butyl alcohol and ultrasonically dispersed. A few drops of the resulting suspension were deposited on a carbon-coated copper grid. The selected-area electron diffraction (SAED) and high-resolution transmission electron microscopy (HRTEM) experiments were performed on a JEOL JEM 3000F microscope operating at 300 kV (double tilt $\pm 20^\circ$) (point resolution 0.17 nm), fitted with an X-ray energy dispersive spectroscopy (XEDS) microanalysis system (OXFORD INCA) and an ENFINA spectrometer with an energy resolution of 1.3 eV. The atomic ratio of the La, Nb(Ta) and Zr metals was determined by XEDS in at least 20 crystals of each sample.

Electrical characterization

The electrical behavior of the oxides in air and at different temperatures was evaluated by AC impedance spectroscopy. Pellets of 10 mm diameter and 1.2 mm thickness were prepared by pressing the powder samples and sintering them at 1473 K. Electrodes were made by coating opposite pellet faces with platinum paste and heating to 1123 K. The impedance experiments were carried out using a frequency response analyzer Solartron 1255A with a dielectric interface 1296. Measurements were performed in air with heating and cooling cycles between 298 and 473 K, in the frequency range of 10^{-1} to 10^7 Hz, and an excitation voltage of 50 mV.

Electrochemical characterization

To study the electrochemical stability of the oxides, positive electrodes were prepared from a mixture of the studied oxide, Super C65 conductive carbon, and PVDF binder in an 80 : 10 : 10 weight ratio. Following prolonged stirring, slurries elaborated with NMP as a solvent were cast onto thin copper foil. Disc electrodes with 12 mm diameter were cut and dried at 353 K for 24 h under vacuum. The typical mass load of active material was 1.5–2 mg cm⁻² in every electrode. A lithium metal disc was used as the negative electrode. The electrolyte was 1 M LiPF₆ in 1 : 1 v/v ethylene carbonate (EC) : dimethyl carbonate (DMC) using Whatman GF/D glass fiber as a separator. Cell assembly was performed in an argon-filled glove box (H₂O and O₂ content < 0.1 ppm). All electrochemical tests were performed in CR2032 coin cells at 298 K. Cyclic voltammetry was performed at a scan rate of 0.50 mV s⁻¹ in the 3.0–0.0 V and 3.0–5.0 V potential ranges.

Results and discussion

Crystal structure and microstructure

Powder X-ray diffraction performed on the compounds La_{0.29}Li_{0.12+x}Nb_{1-x}Zr_xO₃ and La_{0.29}Li_{0.12+x}Ta_{1-x}Zr_xO₃, showed that only samples with $x = 0.05$ and 0.1 (the Nb-oxides named LLNZ05 and LLNZ10, and the Ta-oxides named LLTaZ05 and LLTaZ10) are single phases. The corresponding powder X-ray

diffraction patterns (Fig. S1 in the ESI†) show the characteristic diffraction maxima of the perovskite structure. Besides, extra reflections related to the $\sqrt{2}a_p \times \sqrt{2}a_p \times 2a_p$ superstructure are observed (a_p refers to the lattice parameter of the cubic perovskite). The unit cell has been considered taking into account the weak modulation of the crystal structure observed in the SAED patterns and HRTEM images of crystals of the studied oxides (see below). The double parameter results from the layered ordering of the La³⁺ and Li⁺ cations and vacancies (alternation of (001) planes with A-vacancies and (001) planes containing mainly La³⁺ and Li⁺ cations) and the $\sqrt{2}$ factors related to modulation of the tilting of the anion-octahedra sublattice in combination with compositional modulation along the [110]_p direction. The atomic ratio of the La, Nb(Ta) and Zr metals has been determined by XEDS in TEM mode, finding good agreement between experimental and nominal composition in all the crystals of the samples (Table S1 in the ESI†). The lattice parameters have been obtained from Le Bail profile fitting of the XRD patterns (Table S2†). In the case of the samples of composition corresponding to values of x higher than 0.1, secondary phases were detected in addition. The hindrance to obtaining oxides with higher Zr-content under the synthesis conditions used in this work might be related to the cation-vacancy ordering within the crystal structure, since higher Zr-content implies partial filling of the empty (001)-layers with Li-atoms, thus affecting the lamellar ordering of La, Li and vacancies that seems to stabilize the crystal structure.

Fig. 2 shows HRTEM images and the corresponding SAED pattern or Fourier Transform, representative of crystals of both the La_{0.29}Li_{0.22}Nb_{1-x}Zr_xO₃ and La_{0.29}Li_{0.22}Ta_{1-x}Zr_xO₃ studied oxides in illustrative orientations. Diffraction patterns have been indexed according to the cubic perovskite structure ($a_p \approx 4 \text{ \AA}$) (see the ESI†). In the SAED pattern along [100]_p (Fig. 2a), in addition to the Bragg-reflections characteristic of the perovskite, $G_p \pm 1/2(001)^*$ diffraction maxima associated with layered ordering of the La, Li and vacancies along the [001]_p direction are detected, in agreement with the XRD results. The contrast differences observed in the HRTEM image (Fig. 2b) clearly show periodicity in accordance with doubling of the perovskite unit cell ($2a_p$). The SAED pattern along the [001]_p zone axis and the corresponding HRTEM image are shown in Fig. 2c and d, respectively for a crystal of La_{0.29}Li_{0.22}Nb_{0.9}Zr_{0.1}O₃. Four faint reflections in a cross-like arrangement are present at $G_p \pm 1/2(110)^*$ with arms parallel to [100]_p and [010]_p directions. The $G_p \pm 1/2(110)^*$ reflections are associated with the tilting of the octahedral network and the splitting of these reflections into four has been ascribed to the formation of antiphase domains of the twinning of the tilting system in perovskites that present layered-type ordering of two different cations (lanthanide and alkaline atoms) in the A-positions of the structure.^{25–28,31–37} We should mention at this point that, in the case of the Ta compounds, SAED patterns have not given us experimental evidence of the presence of reflections at $G_p \pm 1/2(110)^*$, probably due to their very low intensity. In addition to the tilting-modulation, in some of these perovskite-type oxides,^{25,27,36,37} compositional modulations have been revealed by means of scanning transmission electron microscopy



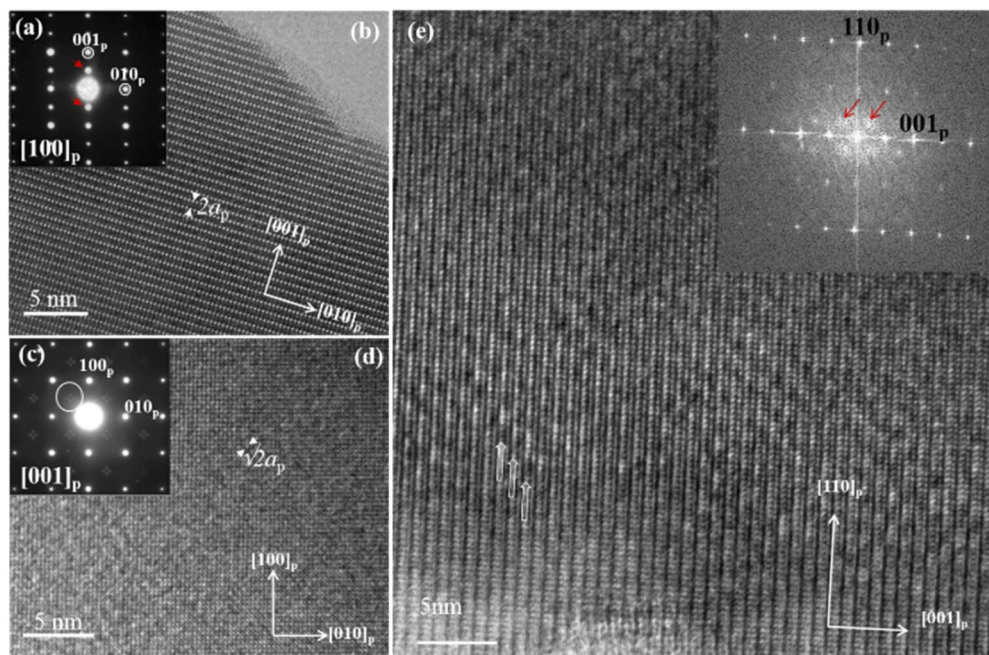


Fig. 2 (a) SAED pattern of a crystal of $\text{La}_{0.29}\text{Li}_{0.22}\text{Nb}_{0.9}\text{Zr}_{0.1}\text{O}_3$ in the $[100]_p$ zone axis, red arrows pointing at $G_p \pm 1/2(001)^*$ extra diffraction maxima. (b) HRTEM image of the crystal in (a). (c) SAED pattern of a crystal of $\text{La}_{0.29}\text{Li}_{0.22}\text{Nb}_{0.9}\text{Zr}_{0.1}\text{O}_3$ in the $[001]_p$ zone axis. The four faint reflections in the cross-like arrangement at $G_p \pm 1/2(110)^*$ are encircled in white. (d) HRTEM image of the crystal in (c). (e) HRTEM image of a crystal of $\text{La}_{0.29}\text{Li}_{0.22}\text{Ta}_{0.9}\text{Zr}_{0.1}\text{O}_3$ in the $[-110]_p$ orientation. Periodic contrast variations are observed in the occupied $(00l)$ planes (white arrows). The inset shows the corresponding Fourier transform and red arrows point at diffuse maxima at odd multiples of $1/4d^*(001)_p$ and $\sim 1/7d^*(110)_p$.

(STEM) in combination with energy electron loss spectroscopy (EELS). Thus, in the $\text{La}_{(1/3)-x}\text{Li}_{3x}\text{NbO}_3$ system, the compositional modulation along the $[110]_p$ direction has been reported to be a consequence of the La, Li and vacancy ordering within the occupied $(00l)$ planes.^{25,27} Fig. 2e shows the HRTEM image of a crystal of $\text{La}_{0.29}\text{Li}_{0.22}\text{Ta}_{0.9}\text{Zr}_{0.1}\text{O}_3$ in the $[-110]_p$ orientation. Subtle contrast periodic variations in the occupied (001) planes are clearly observed. In the corresponding FFT, diffuse maxima at odd multiples of $1/4d^*(001)_p$ and $\sim 1/7d^*(110)_p$ are shown and this information, together with the contrasts observed in the image, suggests the same compositional modulation as that described for $\text{La}_{(1/3)-x}\text{Li}_{3x}\text{NbO}_3$. It must be emphasized that all the oxides of both the Nb and Ta systems present similar SAED and HRTEM features, although the extra reflections are weaker in Ta compounds.

Ionic conductivity

The Li-ion conductivity of the LLNZ05, LLNZ10, LLTaZ05 and LLTaZ10 oxides has been evaluated from the corresponding Nyquist impedance diagrams and from the Bode diagrams (Z'' vs. f) in the T range 298–473 K. Fig. 3 displays impedance diagrams of measurements taken at 298 and 373 K. The graphs corresponding to LLNO are shown in Fig. S2† for comparison. The diagrams of Fig. 3 show only one semicircle and a spike at the lowest frequencies, which is characteristic of the blocking of the Li^+ ions at the electrodes, except for LLTaZ10. The presence of only one semicircle indicates that the resistance values of both the “bulk” and grain boundaries of the materials are

similar and therefore, only the total electrical resistance can be determined. Two semicircles seem to be distinguished in the impedance diagrams of the LLTaZ10 (Fig. 3d) indicating at least two processes at high and middle frequencies, in addition to the

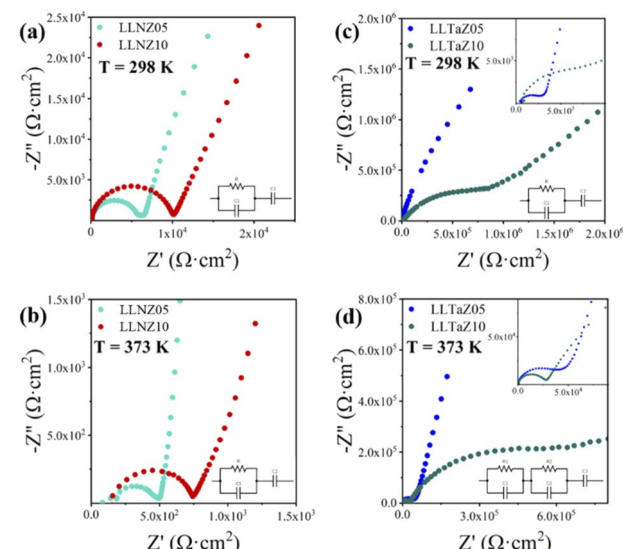


Fig. 3 Complex impedance diagrams of LLNZ05 and LLNZ10 at (a) 298 K and (b) 373 K, and LLTaZ05 and LLTaZ10 at (c) 298 K and (d) 373 K. The insets show the circuital models associated with the impedance results. Please note that according to the explanations in the main text, the circuit represented in (d) models only the behavior of LLTaZ10 at 373 K.



spike at the lowest frequencies. Graphic representations of Z'' and M'' vs. frequency (Fig. 4) allow us to differentiate the processes that take place at different frequencies as far as the resistance and/or the capacitance of these processes have different enough values. In general, the highest frequency processes are associated with the material-bulk electrical behavior and the processes at middle frequencies are associated with grain boundaries; at the lowest frequencies, the ion blocking at the electrodes appears. At room temperature, in the representations of the LLNZ05, LLNZ10, and LLTaZ05 oxides (Fig. 4a–c), only one Z'' and one M'' peak appears at approximately the same frequency (close to 10^5 Hz in the three cases), thus corresponding to the total electrical behavior of the materials, in agreement with Nyquist diagrams. Z'' deeply increases at low frequency due to the high resistance associated with the blocking of Li^+ ions at the electrodes. However, two Z'' peaks are clearly detected in the diagram of the LLTaZ10 oxide at about 10^5 and 1 Hz (Fig. 4d), although only the M'' peak at the highest frequency can be distinguished due to the lower capacitance of this process. The further increase of Z'' at the lowest frequencies is associated to the spike due to the Li-blocking at the electrodes. These representations confirm that both the resistances of bulk and grain boundaries are similar in the LLNZ05, LLNZ10, and LLTaZ05 oxides. However, the LLTaZ10 results show, in addition to the high frequency process of the material bulk, a middle frequency process with higher resistance and capacitance due to grain boundary effects. Table S3† shows resistance, conductivity and capacitance values of the studied oxides at different temperatures as determined from both the Nyquist-impedance and Bode diagrams. The results of the $\text{La}_{0.29}\text{Li}_{0.12}\text{NbO}_3$ (LLNO) oxide prepared for this work are included for comparison. The values correspond to the total resistance (*i.e.*, they include the contribution of both the bulk and grain boundary effects) except for LLTaZ10 for which bulk and grain boundary processes are distinguished at room temperature in the Z'' vs. f diagram (at about 10^5 and 1 Hz respectively). Fig. 5 shows a graphic representation of the variation of the total conductivity with temperature of the oxides, including the results of the LLNO for comparison. The

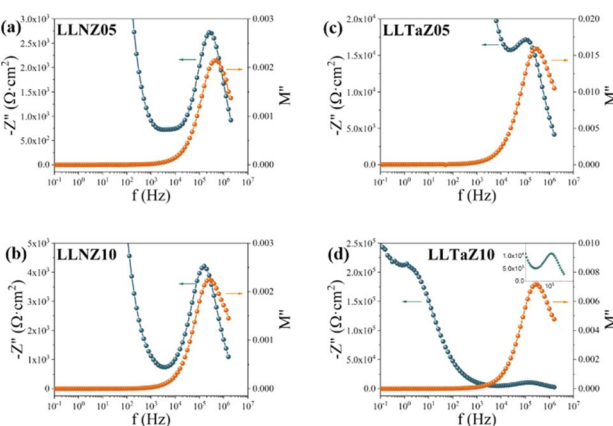


Fig. 4 Z'' and M'' vs. frequency at 298 K of (a) LLNZ05, (b) LLNZ10, (c) LLTaZ05 and (d) LLTaZ10. Inset on (d) shows the enlargement of the peak observed at $\sim 10^5$ Hz.

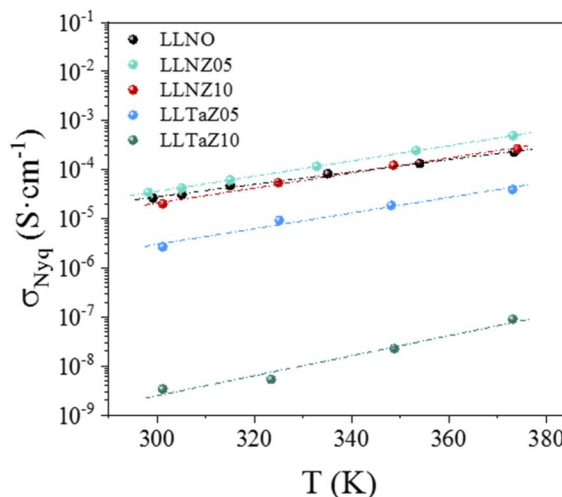


Fig. 5 Variation of total conductivity vs. temperature of the oxides. The results of LLNO have been included for comparison. Conductivity values have been determined from the Nyquist-impedance diagrams.

corresponding activation energies can be found at the end of Table S3.† The obtained values are of the same order as other Li ion conducting perovskite type systems. The Nb-compounds present higher total conductivity than the oxides of the Ti-system. The LLTaZ10 has very low Li-conductivity as a result of the high resistance process at the grain boundaries. The conductivity values of the LLTaZ05, somewhat lower than those of LLNZ10, are in agreement with previous results of the $\text{La}_{(1/3)}-\text{Li}_{3x}\text{TaO}_3$ system that report the highest Li-conductivity at room temperature in the compound corresponding to $x = 0.06$ (7×10^{-6} S cm⁻¹).²⁸ The Li-conductivity increases in the Nb-system by substitution of Nb by Zr and Li in the LLNZ05 due to the increasing number of charge carriers but slightly decreases with higher substitution in LLNZ10 probably due to total occupancy of the conduction-active A-cation vacancies. The results are in agreement with previous conclusions about the characteristics of the grain boundaries in the $\text{La}_{(1/3)}-\text{Li}_{3x}-\text{NbO}_3$ system: the electrical resistance and capacitance values of the grain boundary processes are similar to those of the bulk.^{13,21,22} Moreover, Kawahara *et al.*²² claimed higher Li-conductivity at the grain boundaries than at the bulk in $\text{La}_{0.31}\text{Li}_{0.07}\text{NbO}_3$ due to specific local atomic configurations at the grain boundaries. On the contrary, the different nature of the grain boundaries of the Ti systems, which show strong Li-depletion at the grain boundary regions, leads to higher grain boundary resistances and capacitances.^{23,38}

Electrochemical stability

Along with high ionic conductivity, good electrochemical stability of the solid electrolytes is an additional important criterion to be considered for developing ASSBs. The electrochemical stability of the studied perovskites *versus* lithium has been investigated by cyclic voltammetry of half cells bearing LLNZ05 and LLTaZ05 as the positive electrode. Thus, reduction/oxidation potentials *versus* Li^+/Li are determined. The selection

of these oxides has been based on their highest conductivity in the corresponding systems. Fig. 6a and b show the first four reduction–oxidation waves of LLNZ05 and LLTaZ05 respectively, in the low voltage range 3.0–0.0 V. The formation of the solid electrolyte interphase (SEI) is observed in the first cycle (black line) centered at *ca.* 0.5 V. Subsequent cycles show the reversible processes taking place in these perovskites upon consecutive reduction/oxidation cycles. Electrochemical stability window of the niobate LLNZ05 at low voltage is deduced from Fig. 6a. It shows that cathodic current is negligible down to 2.0 V. Below this potential a broad cathodic peak is developed in the potential range 2.0–0.75 V *vs.* Li⁺/Li, ascribed to the reduction of Nb⁵⁺ to Nb⁴⁺, while another broad peak located at 0.6 V is consistent with the reduction of Nb⁴⁺ to Nb³⁺ at a much lower voltage.^{39,40} The LLTaZ05 (Fig. 6b) develops one broad cathodic peak located in the potential range 1.3–0.6 V ascribed to the reduction of the Ta⁵⁺ to Ta⁴⁺ redox couple. Interestingly, the cathodic current appears at a significantly lower voltage in the case of LLTaZ05 (below 1.3 V *vs.* Li⁺/Li) compared to the cathodic current in the niobate (below 2.0 V *vs.* Li⁺/Li), evidencing a significant widening of the electrochemical stability window of this oxide compared to the corresponding niobate. Cyclic voltammetry studies performed in the high voltage range (3.0–5.0 V) demonstrate the remarkable electrochemical stability of both compounds. Fig. 6c and d show that anodic current is negligible up to 4.8 V in both compounds. Even though a significant overpotential compared to the calculated thermodynamic equilibrium potential is expected in some oxides for the oxidation reaction processes, likely due to having slow kinetics, LLNZ05, LLNZ10 and LLTaZ05 are among the most stable oxides at high voltages reported. Blanks were run at an identical sweep rate of 0.5 mV s⁻¹ (Fig. S3†) in the low potential (0.0–3.0 V *vs.* Li⁺/Li, Fig. S3b†) and high potential range (3.0–5.0 V *vs.* Li⁺/Li, Fig. S3d†). Comparison of the cyclic voltammogram of LLTaZ05 and its blank in the low voltage range (0.0–3.0 V, Fig. S3a and b†) confirms that the cathodic current below 1.3 V *vs.* Li⁺/Li is due to the active material

LLTaZ05 and thus, represents the lower electrochemical stability limit. On the other hand, in the high voltage range, the comparison of the anodic current with that of the corresponding blank cell (Fig. S3c and d†) confirms that the higher electrochemical stability limit is around 4.8 V.

Comparison of the ion-conductivity and electrochemical stability of LLNZ05, LLNZ10 and LLTaZ05 with other Li-ion conducting oxides confirms the valuable behavior of these new materials as solid electrolytes.^{4,6} As example, the total Li-conductivity in the LLTO system is of the order of 10⁻⁵ S cm⁻¹ at room temperature and the calculated electrochemical window is in between 1.7 V (reduction potential *vs.* Li⁺/Li) and 4.2 V (oxidation potential *vs.* Li⁺/Li).⁶ The room temperature Li-conductivity in LLNZ05 and LLNZ10 is of the same order of magnitude as in LLTO and somewhat lower in LLTaZ05. However, the electrochemical window is significantly wider in LLTaZ05 (1.3–4.8 V). Interestingly, in LLTaZ05 the reduction of Ta⁵⁺ to Ta⁴⁺ occurs at a much lower potential than the reduction of Ti⁴⁺ to Ti³⁺ in Li₄Ti₅O₁₂ (1.55 V) opening the possibility of using these Ta-based oxides as an electrolyte with the Li₄Ti₅O₁₂ anode, one of the few anodes marketed to date besides graphite.

Conclusions

Single phase oxides of the systems La_{0.29}Li_{0.12+x}Nb_{1-x}Zr_xO₃ and La_{0.29}Li_{0.12+x}Ta_{1-x}Zr_xO₃ (*x* = 0.05 and 0.1) have been synthesized. Substitution of Nb or Ta by Zr and Li is limited to *x* = 0.1 when the oxides are prepared by the conventional ceramic method. The obtained oxides present a perovskite-related structure with ordering of the A-cation vacancies, like in the crystal structure of the parent La_{0.29}Li_{0.12}NbO₃ compound, in such a way that (00*l*) layers of A-cation vacancies alternate with layers of La, Li and vacancies. Ordering of cation vacancies seems to limit the Li-doping to that corresponding to *x* = 0.1, thus frustrating the filling of the empty (00*l*) layers with Li-atoms. The LLNZ05, LLNZ10 and LLTaZ05 oxides are potential electrolytes for Li-ASSBs because of their valuable electrical and electrochemical behavior and low grain boundary resistances. LLNZ05 shows slightly higher conductivity and a similar electrochemical window compared to the parent LLNO compound. However, LLTaZ05 exhibits lower Li-conductivity though still in the range of solid electrolytes but remarkably presents a wider electrochemical window (~1.3–4.8 V *vs.* Li⁺/Li) currently reported for solid Li-conductor oxides.

Data availability

The data supporting this article have been included as part of the ESI.†

Author contributions

Ester García-González: methodology, validation, investigation, writing – review & editing, visualization. Rafael Marín-Gamero: methodology, validation, formal analysis, investigation, writing – review & editing, visualization. Miguel Kuhn-Gómez: investigation. Alois Kuhn: methodology, validation, formal analysis,

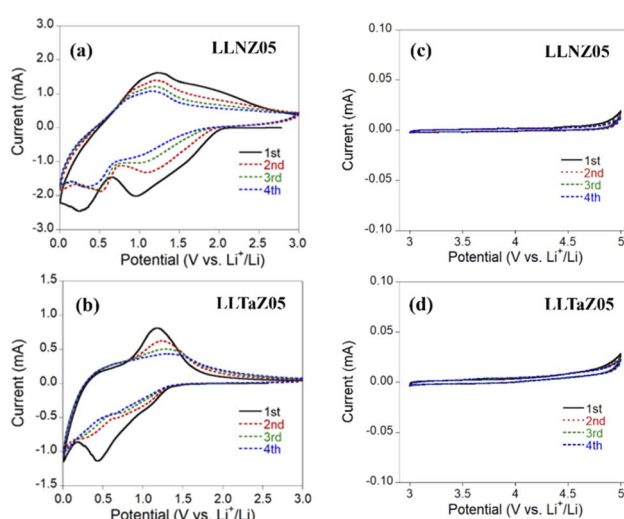


Fig. 6 Cyclic voltammograms of LLNZ05 and LLTaZ05 in the 0–3 V voltage range (a and b) and in the 3.0–5.0 V voltage range (c and d).



investigation, writing – review & editing, visualization. Flaviano García-Alvarado: methodology, validation, formal analysis, investigation, writing – review & editing, visualization. Susana García-Martín: conceptualization, methodology, validation, formal analysis, investigation, writing – original draft, visualization, supervision, project administration.

Conflicts of interest

There are no conflicts to declare.

Acknowledgements

This work has been supported by the Spanish MCIN/AEI/10.13039/501100011033 with the projects PID2022-139039OB-C22, PID2022-139039OB-C21, PID2019-106662RB-C44, and PID2019-106662RB-C41. The authors acknowledge the ICTS-CNME at UCM for electron microscopy facilities.

Notes and references

- 1 C. Sun, J. Liu, Y. Gong, D. P. Wilkinson and J. Zhang, *Nano Energy*, 2017, **33**, 363–386.
- 2 T. Famprakis, P. Canepa, J. A. Dawson, M. S. Islam and C. Masquelier, *Nat. Mater.*, 2019, **18**, 1278–1291.
- 3 Z. Wu, Z. Xie, A. Yoshida, Z. Wang, X. Hao, A. Abudula and G. Guan, *Renewable Sustainable Energy Rev.*, 2019, **109**, 367–385.
- 4 K. J. Kim, M. Balaish, M. Wadaguchi, L. Kong and J. L. M. Rupp, *Adv. Energy Mater.*, 2021, **11**, 2002689.
- 5 R. Chen, Q. Li, X. Yu, L. Chen and H. Li, *Chem. Rev.*, 2020, **120**, 6820–6877.
- 6 Y. Zhu, X. He and Y. Mo, *ACS Appl. Mater. Interfaces*, 2015, **7**, 23685–23693.
- 7 K. Tuo, C. Sun and S. Liu, *Electrochem. Energy Rev.*, 2023, **6**, 17.
- 8 Y. Inaguma, C. Liquan, M. Itoh, T. Nakamura, T. Uchida, H. Ikuta and M. Wakihara, *Solid State Commun.*, 1993, **86**, 689–693.
- 9 F. García-Alvarado, A. Várez, E. Morán and M. A. Alario-franco, *Phase Transitions*, 1996, **58**, 111–120.
- 10 Y. J. Shan, L. Chen, Y. Inaguma, M. Itoh and T. Nakamura, *J. Power Sources*, 1995, **54**, 397–402.
- 11 O. Bohnke, C. Bohnke and J. L. Fourquet, *Solid State Ionics*, 1996, **91**, 21–31.
- 12 Y. Kawakami, H. Ikuta and M. Wakihara, *J. Solid State Electrochem.*, 1998, **2**, 206–210.
- 13 S. García-Martín, J. M. Rojo, H. Tsukamoto, E. Morán and M. A. Alario-Franco, *Solid State Ionics*, 1999, **116**, 11–18.
- 14 A. Morata-Orrantia, S. García-Martín, E. Morán and M. Á. Alario-Franco, *Chem. Mater.*, 2002, **14**, 2871–2875.
- 15 C. H. Chen, S. Xie, E. Sperling, A. S. Yang, G. Henriksen and K. Amine, *Solid State Ionics*, 2004, **167**, 263–272.
- 16 R. Yu, Q.-X. Du, B.-K. Zou, Z.-Y. Wen and C.-H. Chen, *J. Power Sources*, 2016, **306**, 623–629.
- 17 B. Huang, B. Xu, Y. Li, W. Zhou, Y. You, S. Zhong, C.-A. Wang and J. B. Goodenough, *ACS Appl. Mater. Interfaces*, 2016, **8**, 14552–14557.
- 18 M. Amores, H. El-Shinawi, I. McClelland, S. R. Yeandel, P. J. Baker, R. I. Smith, H. Y. Playford, P. Goddard, S. A. Corr and E. J. Cussen, *Nat. Commun.*, 2020, **11**, 6392.
- 19 A. Jondrian, R. Peng, D. Davies and E. McCalla, *Chem. Mater.*, 2023, **35**, 6227–6234.
- 20 Y. Fujiwara, K. Hoshikawa and K. Kohama, *J. Cryst. Growth*, 2016, **433**, 48–53.
- 21 X. Hu, C. A. J. Fisher, S. Kobayashi, Y. H. Ikuhara, Y. Fujiwara, K. Hoshikawa, H. Moriwake, K. Kohama, H. Iba and Y. Ikuhara, *Acta Mater.*, 2018, **156**, 379–388.
- 22 K. Kawahara, R. Ishikawa, K. Nakayama, T. Higashi, T. Kimura, Y. H. Ikuhara, N. Shibata and Y. Ikuhara, *J. Power Sources*, 2019, **441**, 227187.
- 23 J.-F. Wu and X. Guo, *Phys. Chem. Chem. Phys.*, 2017, **19**, 5880–5887.
- 24 S. García-Martín, M. A. Alario-Franco, H. Ehrenberg, J. Rodríguez-Carvajal and U. Amador, *J. Am. Chem. Soc.*, 2004, **126**, 3587–3596.
- 25 X. Gao, C. A. J. Fisher, Y. H. Ikuhara, Y. Fujiwara, S. Kobayashi, H. Moriwake, A. Kuwabara, K. Hoshikawa, K. Kohama, H. Iba and Y. Ikuhara, *J. Mater. Chem. A*, 2015, **3**, 3351–3359.
- 26 S. García-Martín and M. Á. Alario-Franco, *J. Solid State Chem.*, 1999, **148**, 93–99.
- 27 X. Hu, S. Kobayashi, Y. H. Ikuhara, C. A. J. Fisher, Y. Fujiwara, K. Hoshikawa, H. Moriwake, K. Kohama, H. Iba and Y. Ikuhara, *Acta Mater.*, 2017, **123**, 167–176.
- 28 K. Mizumoto and S. Hayashi, *J. Ceram. Soc. Jpn.*, 1997, **105**, 713–715.
- 29 A. Le Bail, H. Duroy and J. L. Fourquet, *Mater. Res. Bull.*, 1988, **23**, 447–452.
- 30 J. Rodríguez-Carvajal, *Phys. B*, 1993, **192**, 55–69.
- 31 Y. Sakai, D. Urushihara, T. Asaka, K. Fukuda, Z. Yang, N. Tanibata, H. Takeda and M. Nakayama, *Phys. Status Solidi*, 2022, **259**, 2100561.
- 32 M. Labeau, I. E. Grey, J. C. Joubert, J. Chenevas, A. Collomb and J. C. Guitel, *Acta Crystallogr., Sect. B: Struct. Sci.*, 1985, **41**, 33–41.
- 33 S. García-Martín, F. García-Alvarado, A. D. Robertson, A. R. West and M. A. Alario-Franco, *J. Solid State Chem.*, 1997, **128**, 97–101.
- 34 R. L. Withers, L. Bourgeois, A. Snashall, Y. Liu, L. Norén, C. Dwyer and J. Etheridge, *Chem. Mater.*, 2013, **25**, 190–201.
- 35 A. M. Abakumov, R. Erni, A. A. Tsirlin, M. D. Rossell, D. Batuk, G. Nénert and G. Van Tendeloo, *Chem. Mater.*, 2013, **25**, 2670–2683.
- 36 S. García-Martín, E. Urones-Garrote, M. C. Knapp, G. King and P. M. Woodward, *J. Am. Chem. Soc.*, 2008, **130**, 15028–15037.
- 37 S. García-Martín, G. King, E. Urones-Garrote and P. M. Woodward, *J. Am. Chem. Soc.*, 2021, **143**, 19121–19127.
- 38 S. García-Martín, A. Morata-Orrantia, M. H. Aguirre and M. Á. Alario-Franco, *Appl. Phys. Lett.*, 2005, **86**, 43110.
- 39 R. Zheng, S. Qian, X. Cheng, H. Yu, N. Peng, T. Liu, J. Zhang, M. Xia, H. Zhu and J. Shu, *Nano Energy*, 2019, **58**, 399–409.
- 40 X. Xiong, L. Yang, G. Liang, C. Wang, G. Chen, Z. Yang and R. Che, *Adv. Funct. Mater.*, 2022, **32**, 2106911.

